Three-dimensional micron-porous graphene foams for lightweight current collectors of lithium-sulfur batteries

Lu, Liqiang; De Hosson, Jeff Th. M.; Pei, Yutao

Published in:
Carbon

DOI:
10.1016/j.carbon.2018.12.103

Publication date:
2019

Carbon 144 (2019) 713–723

Contents lists available at ScienceDirect

Carbon

journal homepage: www.elsevier.com/locate/carbon

Three-dimensional micron-porous graphene foams for lightweight current collectors of lithium-sulfur batteries

Liqiang Lu [a], Jeff Th. M. De Hosson [b], Yutao Pei [a, *]

[a] Department of Advanced Production Engineering, Engineering and Technology Institute Groningen, University of Groningen, Nijenborgh 4, 9747 AG, Groningen, the Netherlands
[b] Department of Applied Physics, Zernike Institute for Advanced Materials, University of Groningen, Nijenborgh 4, 9747AG, Groningen, the Netherlands

ARTICLE INFO

Article history:
Received 23 July 2018
Received in revised form
20 December 2018
Accepted 28 December 2018
Available online 29 December 2018

Keywords:
Graphene foam
Micron-porous graphene
Current collectors
Lithium-sulfur batteries
Energy storage devices

ABSTRACT

This paper reports a three-dimensional (3D) stochastic bicontinuous micron-porous graphene foam (3D-MPGF) developed as lightweight binder-free current collectors for sulfur cathodes of lithium-sulfur batteries. 3D-MPGF is synthesized by a facile process that originally combines the synthesis of porous metals by the reduction of metallic salts and chemical vapor deposition (CVD) growth of graphene in a continuous route. 3D-MPGF presents micron-porous structure with both interconnected tubular pores and nontubular pores of sizes from hundreds nanometers to several microns. By adjusting CVD time, the thickness of graphene wall is tunable from few atomic layers to ten layers. Raman results prove a high crystalline of 3D-MPGF. Attributed to the low density and high quality, 3D-MPGF can be used as promising lightweight binder-free current collectors. The 3D-MPGF loaded with S of 2.5 mg cm^{-2} exhibited an ultrahigh initial capacity of 844 mAh g^{-1} (of electrode), and maintain at 400 mAh g^{-1} after 50 cycles at 0.1C (167 mA g^{-1}). With increasing the loading of S, the electrodes present higher areal capacities. When the loading of S is 13 mg cm^{-2}, the areal capacity of 3D-MPGF/S reaches 5.9 mAh cm^{-2} after 50 cycles at 0.1C. The use of 3D micron-porous graphene foam proves considerably enhanced gravimetric capacity densities (of overall electrode), which can be a direction not only for batteries but also for other energy storage devices.

1. Introduction

Coupled with lithium anode, lithium-sulfur (Li–S) batteries can be regarded as one of the promising next-generation batteries because of the high theoretical gravimetric energy density (~2600 Wh kg^{-1}) and volumetric energy density (~2800 Wh L^{-1}). Sulfur exhibits a high theoretical specific capacity of ~1675 mAh g^{-1}, which is much higher than that of conventional materials of lithium transition metal oxides. More promisingly, the relatively low cost and abundance of sulfur could substantially reduce the cost of batteries in the future [1,2]. However, Li–S batteries suffer from multiple issues and challenges, such as the poor electronic and ionic conductivity of sulfur and its fully discharged product Li_2S, dissolution of polysulfides and the so-called "shuttling effect" of polysulfides between the electrodes, and large volume expansion of sulfur during discharging. These severely result in an inefficient use of sulfur and fast capacity decay [1–23]. Considerable efforts have been made to address these challenges through composite electrodes that contain sulfur in a conductive porous hosts such as porous carbon (carbon nanotube, graphene), polymers, metal oxides and metal sulfides [4–12]. Nevertheless, the limited sulfur loading (less than 2.0 mg cm^{-2}) and sulfur contents (lower than 70 wt%) usually cause low areal capacities [13].

Yet another issue that is usually neglected is that other components of composite electrodes, such as binders and aluminum current collectors (CC) (~5.4 mg cm^{-2} for the foil with a thickness of 20 μm), severely reduce the specific capacities of overall electrodes and energy densities of whole cells. These problems dramatically diminish the advantages of high capacity of sulfur and high-energy density of Li–S batteries. The advancements in lightweight and binder-free current collector are promising for both Li–S batteries as well as other energy storage devices. Integration of active materials (such as S) and porous current collectors together provides a solution. Porous carbonaceous materials are thus attracting great attentions due to the high electric conductivity, low densities, good mechanical properties and stable chemical properties. Various

* Corresponding author.
E-mail address: y.pei@rug.nl (Y. Pei).

https://doi.org/10.1016/j.carbon.2018.12.103

carbon materials including carbon nanotube, carbon nanofibers, pyrolysis carbon networks from biomass, and porous graphene are developed for binder-free current collectors [14–20].

Three-dimensional (3D) porous graphene foams (3D-PGF) are those of most promising porous current collectors. 3D-PGF can be built of two-dimensional (2D) graphene layers and submillimetre-sized pores in between [21,22]. These 3D foam structures show promising properties such as lightweight, good electronic and thermal conductivity, high surface area, and providing pathways for ionic transport. 3D-PGF also exhibits good mechanical properties like high strength, stiffness, and damage tolerance properties. Owning to the abovementioned properties, 3D-PGF has become a potential material as current collectors for batteries and supercapacitors [11,12,23,24], delivered higher specific capacities than that of using Al or Cu CC electrodes. 3D graphene foam can be as current collectors for both cathodes and anodes of lithium–ion batteries [25–27]. Regarding the application of porous graphene for Li–S batteries, few work have demonstrated the improved areal capacities and cyclic performances by using 3D graphene foams [6,28]. To achieve high gravimetric density of the overall sulfur electrodes and increase the energy density of Li–S cells, the porous structure, sulfur loading and electrochemical properties of graphene foam/sulfur electrodes require thorough investigations.

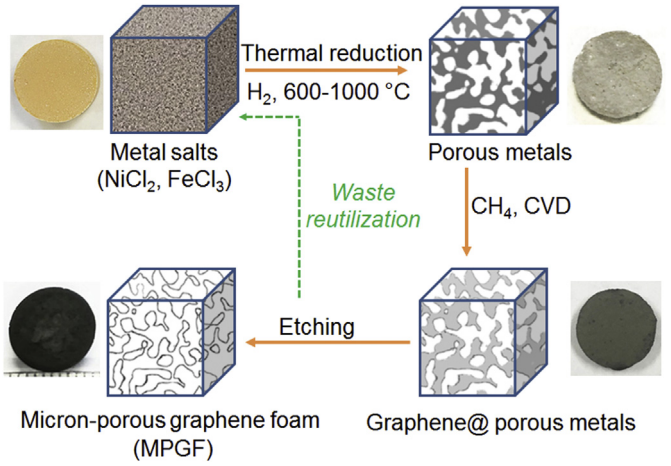

Fig. 1. Schematic illustration of the synthesis of micron-porous graphene foam from metallic salt precursor. The overall process contains three steps: thermal reduction of metallic salts, CVD growth of graphene in porous metal template and removal of the metal template. The photos show a nickel chloride chip, micron-porous Ni chip, graphene coated micron-porous Ni chip and micron-porous graphene foam chip of 13 mm diameter, respectively, made in each step. (A colour version of this figure can be viewed online.)

Prior to the applications, the synthesis of optimal graphene foam is crucial. At present, the methods for synthesizing 3D porous graphene foam include the assembly of reduced graphene oxides and chemical vapor deposition (CVD) of graphene in porous templates [21,22]. The assembly of (reduced) graphene oxides (GO) for porous graphene is usually performed through freeze-drying, hydrothermal and templating [29]. However, the high content of defects such as rich oxygen groups of GO or rGO usually limits the electric conductivity of porous graphene. Filling GO flakes into porous templates could be time-consuming and inefficient for producing 3D foam due to the relatively big size and slow movement of GO flakes into the pores of templates [6]. In contrast, CVD method may produce high quality porous graphene. During CVD, graphene form on the 3D surface of ligaments of the porous substrate. Thus, the main concerns for producing optimal graphene foam is getting desired porous templates and controlling the growth conditions. Metal oxides such as MgO [30], SiO_2 [23] or CaO [31] were investigated as templates. It was found that the growth rate was rather lower and the defect content of porous graphene was higher than that of using metallic substrates. Commercial Ni foams were often used as templates for the synthesis of high-quality graphene foam electrodes but with huge pores (hundreds microns in size). Although the electric conductivity of such graphene foam is good, the large pores may limit the contacts between active materials and graphene. The mechanical properties of as-obtained free-standing graphene foams were also poor, so

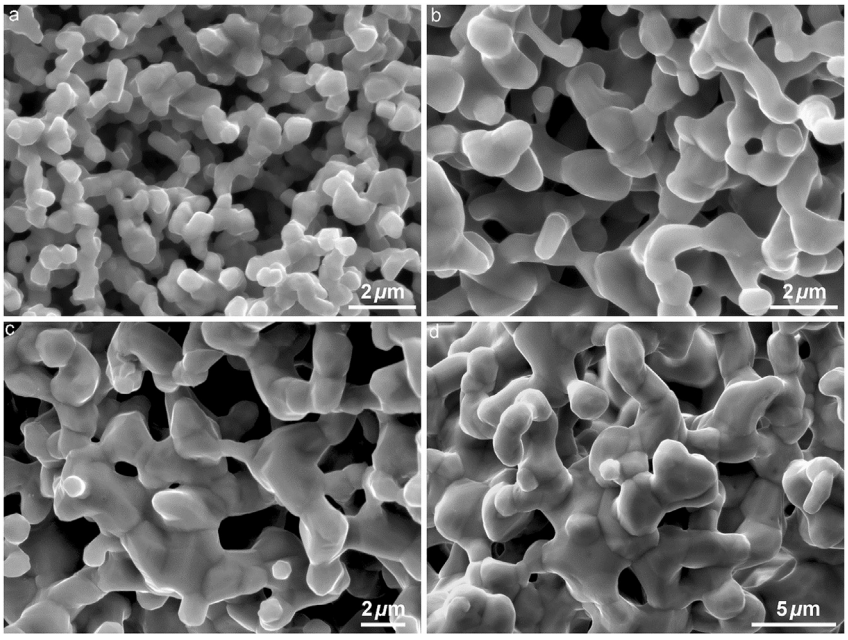

Fig. 2. SEM micrographs showing the microstructure of micron-porous Ni foams reduced from $NiCl_2$ at different temperature: (a) 600°, (b) 700 °C, (c) 800 °C and (d) 900 °C.

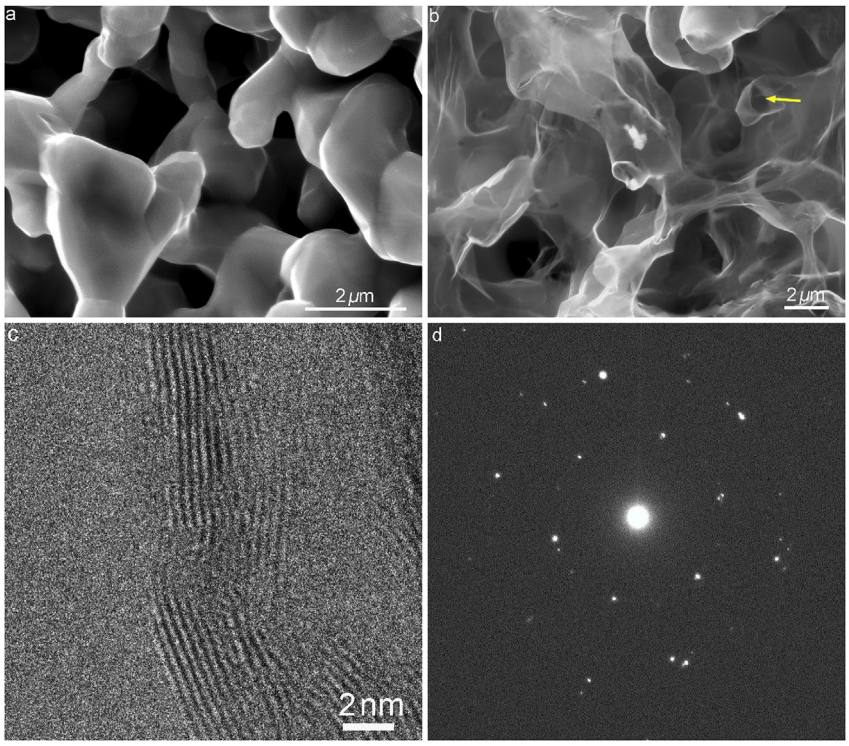

Fig. 3. SEM micrograph showing (a) graphene coated micron-porous Ni foam template and (b) micron-porous graphene foam after etching away porous Ni template with arrows indicating the tubular pores. (c) HR-TEM micrograph and (d) SAED of micron-porous graphene foam. (A colour version of this figure can be viewed online.)

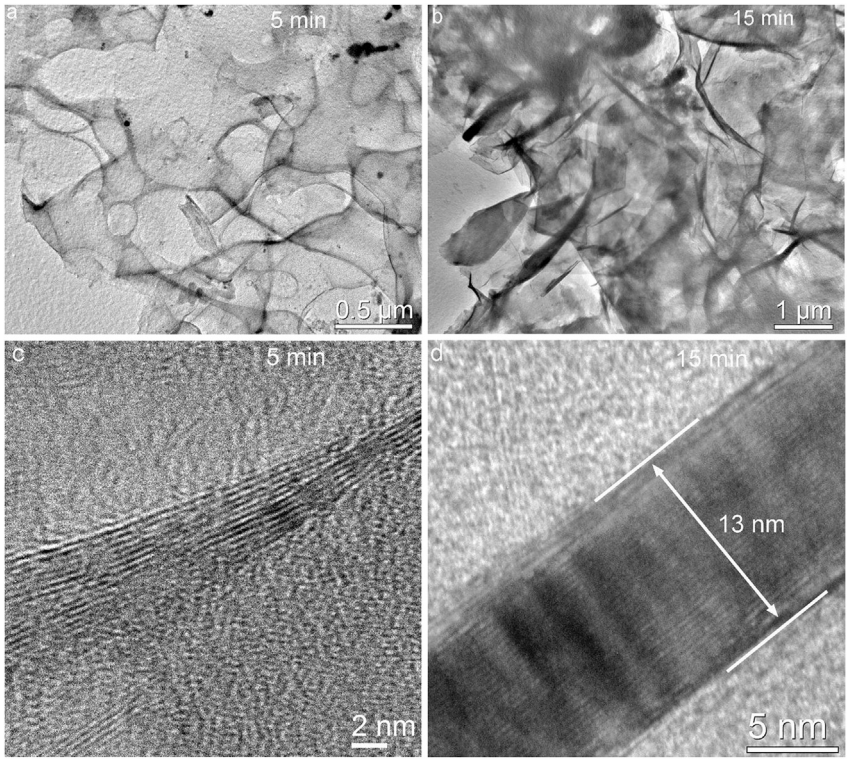

Fig. 4. (a, b) TEM images of micron-porous graphene foam synthesized at 1000 °C for 5 min and 15 min, respectively; (c, d) HR-TEM micrographs showing the thickness of graphene walls of the corresponding micron-porous graphene foams.

polymers such as polydimethylsiloxane (PDMS) are often used as support. Ito et al. and Qin et al. developed nanoporous Ni and Cu templates using dealloying method [32,33]. Smaller pores and good quality of graphene could be obtainable, but the synthesis of nanoporous metals severely increased the costs because of the time-consuming and complicated dealloying processes. For large-scale production of nanoporous graphene there are still many challenges [32,33]. So developing a scalable, low-cost and sustainable approach for the synthesis of micron-porous metals and growth of graphene is of importance.

Inspired by our previous work on the facile synthesis of porous metallic framework by a one-step thermal reduction of metallic salts [34], a combination of synthesis of micron-porous metal and CVD growth of graphene continuously in one-route process may effectively solve the abovementioned problems. Thus, we developed a scalable, facile and sustainable approach for the synthesis of free-standing 3D micron-porous graphene foam (3D-MPGF) for low-density binder-free current collectors of Li–S batteries. The synthesis of 3D-MPGF was fast and cost-effective because of employing a one-route process from metallic salts to graphene coated porous metals. The microstructure of 3D-MPGF is scrutinized by scanning electron microscopy (SEM), transition electron microscopy (TEM) and Raman analysis. The parameters for the synthesis of intermediate porous Ni templates, CVD growth time and temperature are investigated. As an application in energy storage, the electrochemical performances of 3D-MPGF loaded with various contents of S are investigated and compared with conventional S electrodes to stress the advantages of 3D-MPGF current collector for Li–S batteries.

2. Experimental procedures

2.1. Materials preparation and characterization

Typically, 0.35 g $NiCl_2$ powder was pressed into a chip of ϕ~13 mm diameter under 5 t load. The chips were heated to 600 °C and kept for 2 h under the flow of H_2/Ar (15% H_2, 100 sccm), then the temperature was raised to 700–1000 °C and kept for 5–15 min under methane (10% in Ar, 100 sccm) and H_2 (17% in Ar, 200 sccm). The samples were cooled to 700 °C at a cooling rate of ~50 °C min^{-1} and further cooled to room temperature at 20–30 °C min^{-1}. As such, graphene-coated micron-porous Ni foam chips were obtained. Micron-porous graphene foam chips were obtained by etching away the Ni templates in 1 M $FeCl_3$ solution or 2 M HCl solution for 1 day followed by drying at 60 °C. The as-synthesized 3D-MPGF chips have a thickness of ~400 μm.

Slightly different from using $NiCl_2$ as a precursor, iron chloride was firstly hydrogen reduced at 700 °C for 2 h, followed with a CVD at 920 °C for 10 min. After that, the samples were cooled to 700 °C within 10 min, followed with a cooling to the room temperature rapidly under H_2.

The 3D-MPGF-Sx electrodes with different sulfur loadings x in mg cm^{-2} were prepared by drop casting method. Typically, the 3D-MPGF chips were firstly dipped in 2.5 mg mL^{-1} poly(methyl methacrylate) (PMMA) toluene solution for 1 h, then dry at ~100 °C. Thereafter, a certain amount of sulfur/Super P carbon black (CB) dispersion (100 mg mL^{-1} of S in CS_2 with well dispersed CB of 2 mg mL^{-1}) was dropped onto the 3D-MPGF foam in a bottle, and then kept for 1 h. After drying the electrodes, heat them at 155 °C for 12 h under argon protection. The thickness of the 3D-MPGF/S chips after filling with S is the same as that of the 3D-MPGF chips. The sulfur loading x was controlled by the amount of sulfur/CS_2/CB dispersion added into the porous graphene chip. The sulfur content in the 3D-MPGF-S electrodes was calculated according to the mass change of 3D-MPGF before and after sulfur infiltration subtracting the amount of carbon black used. For example, the 3D-MPGF-S13 was synthesized by adding 175 μL of sulfur/CS_2/CB dispersion into the chip followed by drying before heating.

The microstructures of the micron-porous graphene, micron-porous metals and 3D-MPGF-S electrodes were examined by scanning electron microscopy (SEM, Philips FEG-XL30s) and high resolution transmission electron microscopy (HR-TEM, JEOL JEM-2010F operated at 200 kV). Raman spectrum analysis was performed by using laser excitation of 633 nm on a Perkin Elmer Raman station. The specific surface area and pore size of 3D-MPGF and 3D-MPGF-S composites were detected with N_2 adsorption/desorption experiment at 77 K using a Quantachrome Autosorb-3B surface analyzer. The resistivity and electric conductivity of 3D-MPGF and 3D-MPGF-S composites were measured on a four-point-probe tester with using Van der Pauw method [35].

2.2. Electrochemical measurements

The 3D-MPGF-S electrode was assembled in Swagelok-type cells for electrochemical measurements as shown in Scheme 1 in the supplementary information. Lithium chips (ϕ15.6 mm) were used as anodes and Celgard 2500 was used as the separator in the cells. The electrolyte is 1 M lithium bis(tri-fluoromethanesulfonyl) imide

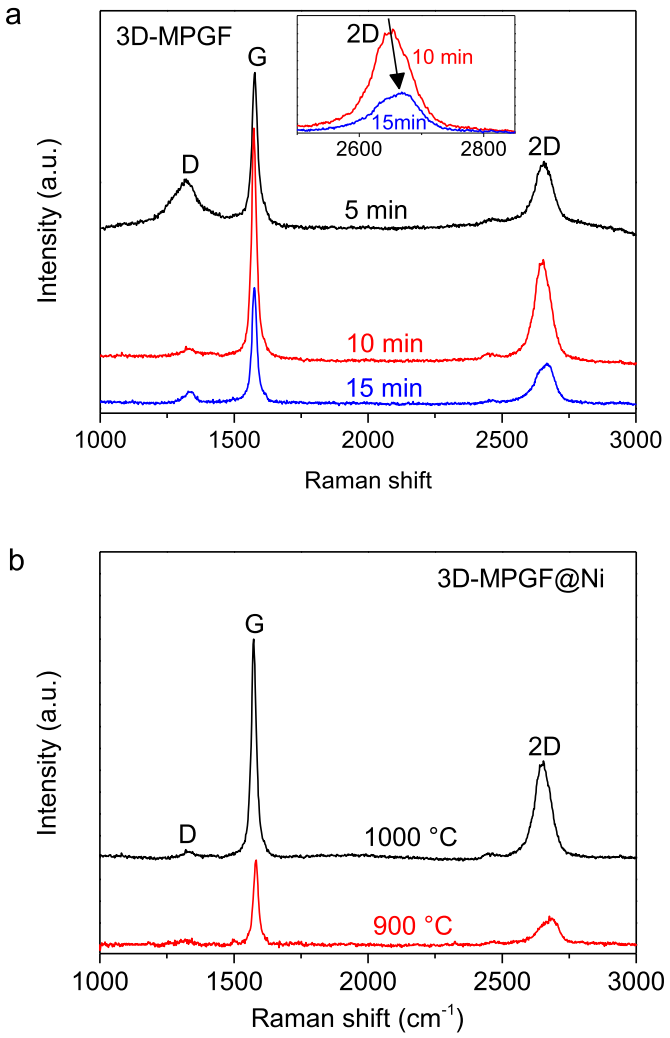

Fig. 5. (a) Raman spectra of 3D-MPGF prepared at 1000 °C for 5, 10 and 15 min, (b) Raman spectra of 3D-MPGF@Ni prepared at 1000 °C and 900 °C for 10 min. (A colour version of this figure can be viewed online.)

(LiTFSI) dissolved in a mixture of 1,3-dioxolane (DOL) and 1,2-dimethoxyethane (DME) (1:1 v/v) with 3.0% lithium nitrate as an additive. The galvanostatic cycling performances were measured at current density of 0.1C (1C = 1673 mA g^{-1}) in the voltage range of 1.7–2.8 V. To fully activate the active materials, the first discharge and charge were performed at 0.05C. The electrochemical impedance spectroscopy was carried out within the frequency from 100 mHz to 100 kHz with AC amplitude of 5 mV on an electrochemical workstation (CH Instruments Model CHI760e).

3. Results and discussion

3.1. Synthesis and microstructure of 3D micron-porous graphene foam

Fig. 1 schematically illustrates the synthesis of micron-porous graphene foam from metallic salts through the one-route process. In the first stage of synthesis, abundant nickel chloride or iron chloride was used, respectively, as precursor. The precursors can be pressed into any desired shape and size, such as a chip shown in Fig. 1. During the hydrogen reduction typically at 600–1000 °C, the chips of metallic salt were reduced to micron-porous metal chips with a slight shrinkage but no change in shape (see the pictures in Fig. 1).

Fig. 2 displays the microstructures of micron-porous Ni reduced from $NiCl_2$ at different temperatures from 600 to 900 °C for 2 h. The micron-porous Ni consists of polycrystalline ligaments that are composed of Ni grains. With increasing the reduction temperature, the thickness of Ni ligaments increases from 0.5 μm to 3 μm, and the size of pores is 0.5–5 μm. The formation of micron-porous structure of Ni from $NiCl_2$ comprises multiple processes including the reduction of $NiCl_2$ to Ni, crystal formation, grain growth, ligaments growth and final configuration of porous structure [34]. The growth of ligaments is preferably at above 600 °C because Ni particles would be obtained otherwise when the temperature is below 600 °C.

After reduction, the temperature was continuously increased to the desired temperature (i.e. 1000 °C) for direct CVD growth of graphene. In this stage, methane or other hydrocarbon gases was introduced for providing carbon atoms. Hydrocarbon molecular catalytically decomposed to provide active C species which adsorbed on the Ni surface. The as-generated carbon atoms diffuse and dissolved into the Ni ligaments because of the high solubility of carbon in Ni [36]. During cooling down the dissolved carbon atoms segregated and precipitated onto the surface of Ni ligaments. In following, graphene nucleated, propagated and grew to cover the Ni ligaments. By controlling the CVD temperature and time, different layer thicknesses and quality of graphene could be achieved. After etching away the underlying micron-porous metal substrates in HCl solution, micron-porous graphene foam were

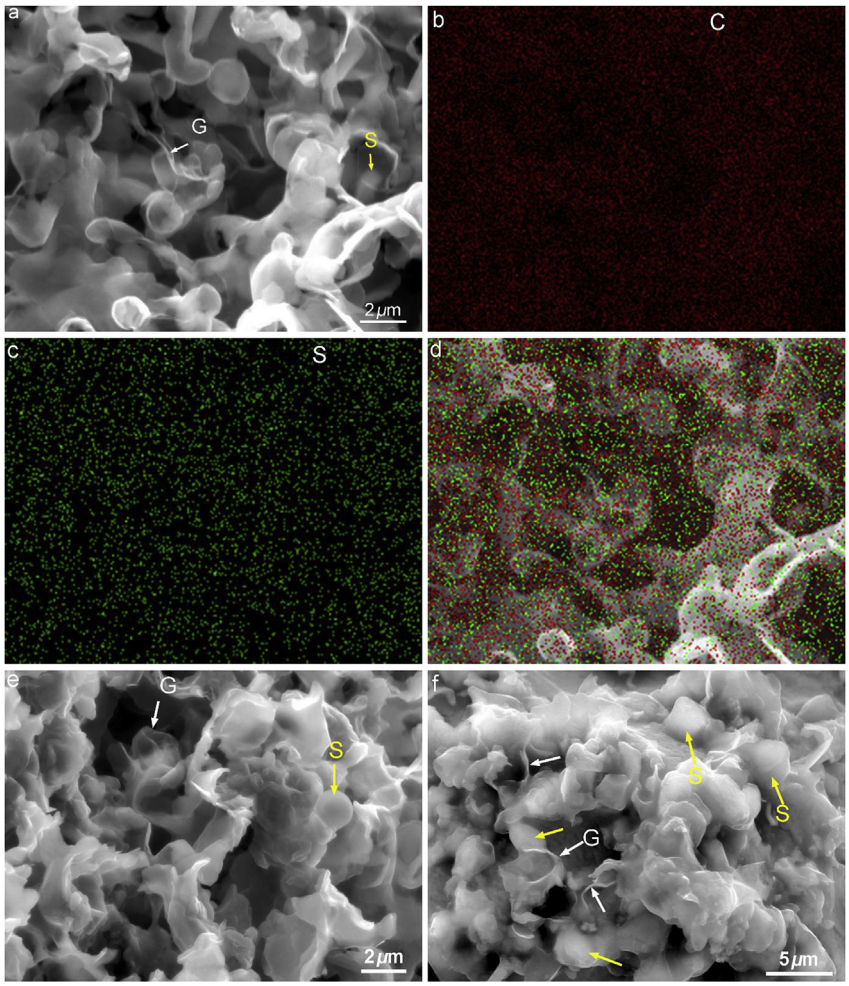

Fig. 6. (a) SEM images of 3D-MPGF-S electrode with 2.5 mg cm^{-2} S, (b–d) EDS mapping of carbon and sulfur, and overlay; SEM image of 3D-MPGF-S electrode with 7 mg cm^{-2} of S (e) and 13 mg cm^{-2} S (f). Graphene is marked with white arrows while sulfur is indicted by yellow arrows. (A colour version of this figure can be viewed online.)

obtained (see the picture in Fig. 1). It should be pointed out that, the waste of nickel chloride from etching of Ni could be easily dried and reutilized for next batch of synthesis without complicated post treatments. It largely reduces the multiple processes from synthesis of porous metals to graphene coated substrates and wastes reuse. The synthesis of porous metal and reutilization of metallic wastes could be sustainable for large-scale production.

Fig. 3a shows graphene film coated micron-porous Ni template. By CVD growth of graphene for 10 min, the size of Ni ligaments seems slightly increased due to the diffusion of Ni atoms at higher temperatures. Graphene film conformably grows on the 3D surface of all Ni ligaments. Fig. 3b reveals the successful synthesis and the microstructure of graphene foam obtained after etching away the Ni templates. The high transparency under electron beam indicates the graphene walls are very thin. The porous structure of graphene remains very well intact without discontinuous flakes after removing the template, indicating the continuous growth of graphene on Ni ligaments. The pores derived from removal of the Ni ligaments exhibit curved tubular channels (marked with arrows). The others are non-tubular pores inherited from the original pores of micron-porous Ni templates. Both of two types of pores of 3DMPGF are continuously interconnected. The size of tubular pores is from submicron to few microns, which are a little smaller than the non-tubular pores. In comparison with those of porous graphene foam synthesized by CVD method with commercial Ni/Cu foams and self-assembly of graphene oxides, the average pore size of 3D-MPGF is much smaller and promising for hosting active materials for the electrodes of batteries and supercapacitors.

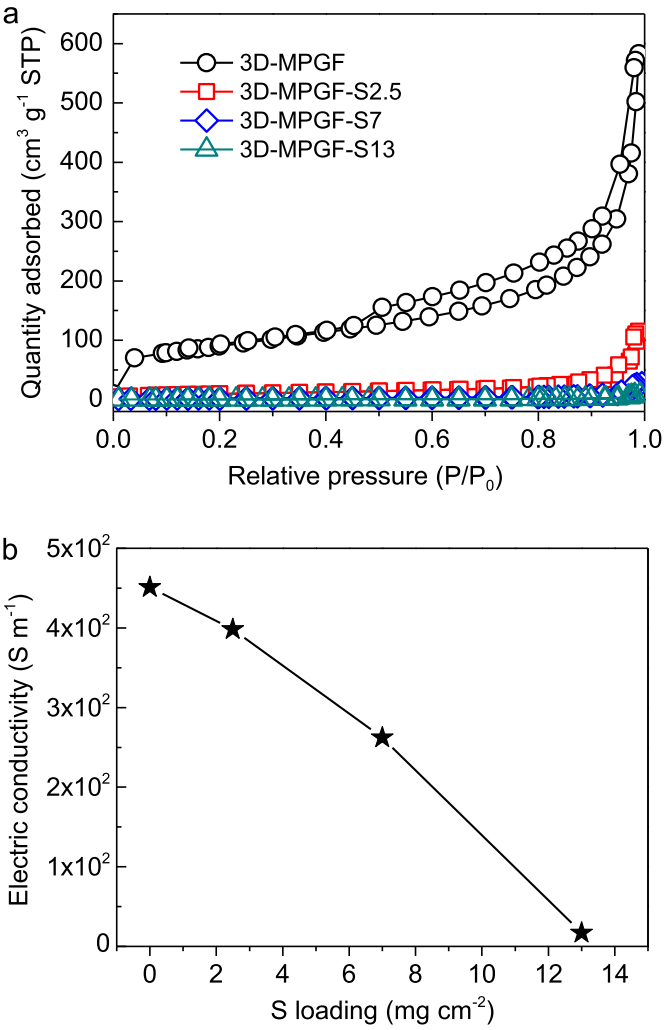

Fig. 7. (a) Nitrogen adsorption–desorption isotherm of 3D-MPGF and 3D-MPGF-S composites, (b) electric conductivity of 3D-MPGF and 3D-MPGF-S composite electrodes with increasing sulfur loadings. (A colour version of this figure can be viewed online.)

The micron-porous graphene foam is mechanically stable with no noticeable claps in the absence of Ni skeletons. It is superb in comparison with previously reported graphene foams which had to be supported by polymers [37]. The average areal weight density of the micron-porous graphene foam chips as shown is only ~1.2 mg cm^{-2} and varied between 0.8 and 1.5 mg cm^{-2}, which is much smaller than that of 20 μm thick Al foil (~5.4 mg cm^{-2}). The average density of micron-porous graphene foam is ~28 mg cm^{-3}, which is only ~1% of the density of Al (2.7 g cm^{-3}). The graphene walls are 7–10 layers determined by HR-TEM as observed in Fig. 3c. The hexagonal SAED pattern of Fig. 3d demonstrates the crystalline of multilayer 3D micron-porous graphene foam.

The wall thickness of the micron-porous graphene foam can be tuned by the CVD time. Fig. 4 shows the microstructures of micron-porous graphene foam synthesized for different CVD periods from 5 min to 15 min at 1000 °C. For 5 min, the 3D-MPGF exhibits similar porous structure with that synthesized in 10 min, but the graphene walls are thinner (~5 layers) as shown in Fig. 4d. It was also found that the 3D-MPGF prepared by 5 min CVD had fracture caused by the shrinkage during drying after etching process and less strength as compared with the 3D-MPGF prepared in 10 min. With prolonging the CVD time to 15 min, the walls become much thicker (~13 nm) as shown in Fig. 4b and can be regarded as thin graphite.

Raman spectroscopy was used to further examine the quality of micron-porous graphene foams, see Fig. 5. All the samples synthesized for 5 min, 10 min and 15 min display D band at ~1325, G bond at ~1570 and 2D band at ~2660 cm^{-1}. The D band is related to the defects activation, and G band is the characteristic of graphite. The I_D/I_G of 3D-MPGF synthesized in 5 min is ~0.31, which is much larger than that of the graphene foams synthesized in 10 min and 15 min (~0.08). The larger I_D/I_G indicates higher content of defects formed in the graphene foam. The crystallite sizes of porous graphene L_a can be estimated according to the following equation [38]:

$$L_a\,(nm) = \left(2.4 \times 10^{-10}\right)\lambda^4\left(\frac{I_D}{I_G}\right)^{-1} \quad (1)$$

where λ is the wavelength of laser beam (in nanometer). By substituting the ratio of I_D/I_G, the crystallite sizes of porous graphene synthesized for 5 min and 10 min is obtained as ~124 nm and ~482 nm, respectively. Thus, with increasing the CVD time from 5 min to 10 min, the crystallite sizes of porous graphene become larger. Beyond 10 min, the crystallinity of graphene remains nearly unchanged. The reason could be due to that shorter growth time leads to smaller crystallite size and thinner wall thickness of the graphene foam, making it easily damaged during etching [39]. The graphene foams prepared in 10 min and 15 min CVD have higher graphitization, which can be proved by the red shift of 2D bond (as shown in the inset of Fig. 5a). We also detect the quality of graphene synthesized at 1000 °C before etching and synthesized at a lower temperature of 900 °C. As can be seen in Fig. 5b, the graphene synthesized at 900 °C also displays weak D band and strong G band, indicating good quality of graphene as well. Nevertheless, the I_D/I_G ratio of graphene coated porous Ni synthesized at 900 °C is 0.08, larger than that of graphene coated porous Ni prepared at 1000 °C (~0.03), revealing more defects in the 3D-MPGF obtained at 900 °C.

It is also interesting to explore other metal salt precursors for making porous graphene, such as the cheap and abundant iron

salts. For a test, iron chloride was firstly hydrogen reduced at 700 °C, then followed with CVD growth of graphene at 920 °C. At this temperature, carbon has a high solubility (~2.14 wt%.) in the face-centered cubic γ-austenite Fe. During cooling, the Fe–C mixture suffers from a phase transformation to body-centered cubic α-ferrite with a lower solubility of C. Carbon atoms precipitated and form graphene coated on iron ligaments of the templates during cooling [40]. After etching away the micron-porous Fe templates, micron-porous graphene foams were also successfully obtained (see the Supplementary information).

3.2. Synthesis and microstructures of 3D-MPGF-S electrodes

Porous graphene can be a promising electrode material for high-energy-density lithium-sulfur batteries. Herein we developed the binder-free and metal-free sulfur cathodes with using 3D-MPGF as current collectors. To achieve high utilization of sulfur, 2 mg mL^{-1} carbon black was added in the sulfur CS_2 solution. 3D-MPGF-S electrodes were obtained by drop casting method. PMMA was used to increase the distribution of sulfur in MPGF. 3D-MPGF-S electrodes with various sulfur loadings were prepared by tuning the amount of sulfur addition. Fig. 6a shows the microstructure of 3D-MPGF-S2.5 electrode with 2.5 mg cm^{-2} S. Due to the PMMA thin coating, the sulfur film distributed very well and conformably attached on the surface of graphene layers. The low loading of sulfur at 2.5 mg cm^{-2} equals to ~63 wt% of sulfur content. Thus the pores are not fully filled in. Fig. 6b–d of energy dispersive spectroscopy (EDS) elements mapping and overlay clearly demonstrate the uniform distribution of sulfur in the micron-porous graphene host. It is assumed that the partially empty volume within the pores can well serve the uptake of Li ions. It is observed in Fig. 6e and f that, with increasing the sulfur loading from 7 to 13 mg cm^{-2} that corresponds to sulfur content from ~82 wt% to ~90 wt%, the pores of 3D-MPGF are gradually filled in. The blocking of pores by sulfur, even though not completely, is more obvious at high loading of 13 mg cm^{-2}.

The specific surface areas (SSA) of the 3D-MPGF and 3D-MPGF-S composites were also analyzed. Fig. 7a shows the N_2 adsorption and desorption isotherms of 3D-MPGF and 3D-MPGF-S composite with various sulfur loadings. It contains a hysteresis loop at P/P_0 between 0.4 and 1 for the sample 3D-MPGF, implying the presence of mesopores. The pure 3D-MPGF exhibits the highest SSA of 316 $m^2 g^{-1}$ calculated based on Brunauer-Emmett-Teller theory. It was found that filling of sulfur significantly reduced the SSA of sulfur composite electrodes. The 3D-MPGF-S electrodes showed a lower SSA of 34.7, 7.0 and 1.8 $m^2 g^{-1}$ for 3D-MPGF-S2.5, 3D-MPGF-S7 and 3D-MPGF-S13, respectively. The lower SSA of 3D-MPGF-S electrodes hints less contact between electrolyte and sulfur, as well as less contact between sulfur and graphene, which could affect the utilization of sulfur.

It is known that the electric conductivity of electrodes is of importance for the utilization of sulfur and the battery performances. The electric conductivities of 3D-MPGF and 3D-MPGF-S electrodes with various sulfur loadings are analyzed, as shown in Fig. 7b. The 3D-MPGF exhibits a rather high electric conductivity of 451 S m^{-1}, which is higher than the previously reported 3D graphene foams [33]. The high electric conductivity of 3D-MPGF can be owing to the higher crystallinity of building multilayer graphene. When introducing 63 wt% sulfur, the electric conductivity of 3D-MPGF-S2.5 electrode shows a lower value of 398 S m^{-1}. With further increasing the sulfur content, the electric conductivity of 3D-MPGF-S electrode drops to 262 and 17 S m^{-1} for 3D-MPGF-S7 and 3D-MPGF-S13, respectively. It should be noted that a significant reduction of the electric conductivity occurs at high loading of sulfur, particularly when the sulfur content is above 82%. This is mainly due to the smaller specific contact area between sulfur and graphene of electrodes with higher S loading in comparison with those of lower S-loading electrodes.

3.3. Electrochemical performances of 3D-MPGF-S electrodes

The electrochemical performances of 3D-MPGF-S electrodes

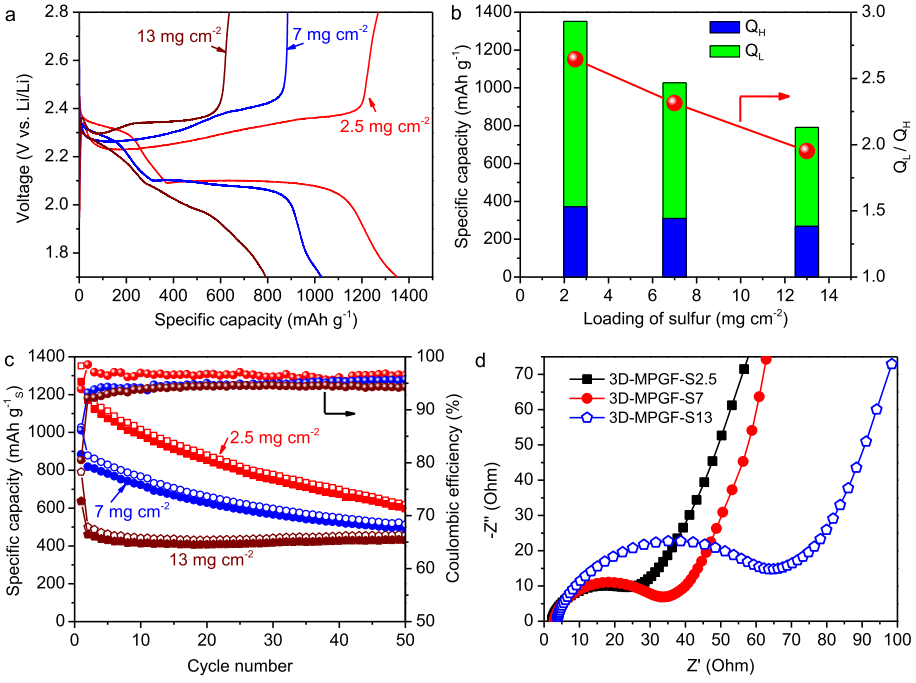

Fig. 8. (a) Galvanostatic charge–discharge profiles of 3D-MPGF-S electrodes with different sulfur loadings; (b) the Q_H, Q_L and ratio of Q_L to Q_H of initial discharge curves of 3D-MPGF-S electrodes with different sulfur loadings; (c) the cyclic performances of 3D-MPGF-S electrodes with different sulfur loadings at 0.1C (167 mA g^{-1}), and the specific capacity calculated based on sulfur; (d) Nyquist plots of the cells employing 3D-MPGF-S electrodes with different loadings of S. (A colour version of this figure can be viewed online.)

with various loadings of sulfur for lithium-sulfur batteries were studied by galvanostatic measurements. Fig. 8a shows the galvanostatic charge-discharge profiles of the 3D-MPGF-S electrodes at 0.05C. Two plateaus can be clearly observed in the discharge process for all the 3D-MPGF-S electrodes. The upper plateau, which contributes ~25% (~419 mAh g^{-1}) of the overall capacity from 2.4 to 2.1 V, corresponds to the conversion from cyclic octa-atomic sulfur (S_8) to long-chain polysulfide anions ($S_8 \rightarrow Li_2S_8 \rightarrow Li_2S_6 \rightarrow Li_2S_4$) [1]. This electrochemical reaction is a kinetically fast solid-to-liquid reaction, which is also associated with the capacity loss and poor electrochemical stability of sulfur electrodes because of the dissolution and diffusion of long-chain polysulfides. The lower plateau, contributing 75% (~1256 mAh g^{-1}) of the overall capacity, at 2.1 to 1.7 V is due to the conversion of long-chain polysulfides to lithium sulfide ($Li_2S_4 \rightarrow Li_2S_2 \rightarrow Li_2S$), which is a slow liquid-to-solid reaction in kinetics. The re-precipitation of lithium sulfides occurred at anodes is also related to the self-discharge and low Coulombic efficiency. The initial discharge and charge capacities of the 3D-MPGF-S2.5 electrode reached 1352 and 1269 mAh g^{-1}, leading to a Coulombic efficiency of 93.9%. With increasing the sulfur loading to 7 mg cm^{-2}, 3D-MPGF-S7 delivered a lower discharge and charge capacities, namely 1027 and 884 mAh g^{-1}, as well as a lower Coulombic efficiency of 86%. The lowest capacities and Coulombic efficiency obtained with the 3D-MPGF-S13 electrode when the sulfur loading is 13 mg cm^{-2}, which are 791 and 637 mAh g^{-1} for discharge and charge and 80% for efficiency, respectively. It is also found with increasing the loading of sulfur, higher overpotentials for both charging and discharging processes occurred. The phenomenon becomes more obvious when increase the S loading from 7 to 13 mg cm^{-2}. The reason for that is mainly due to the lower SSA and electric conductivity of high S-loading electrodes. The above results proved that lower sulfur content results in a higher utilization of S.

The analysis of discharge capacity at the lower plateau (Q_L) and upper plateau (Q_H) provides more information on the utilization of sulfur and polysulfides. Fig. 8b demonstrates the examination of Q_H, Q_L and Q_L/Q_H ratio of 3D-MPGF-S electrodes with different loadings at the initial discharge. It is found under the lowest content of S (~63 wt%), the Q_H and Q_L are the highest (371 and 981 mAh g^{-1}, respectively). However, the real contributions of Q_H and Q_L from sulfur are only 88.5% and 78.1% of the theoretical Q_H and Q_L. With increasing the sulfur loading from 2.5 to 7 and 13 mg cm^{-2}, the Q_H decreases to 310 and 268 mAh g^{-1}, corresponding to 74% and 64% of the theoretical Q_H, respectively. Meanwhile, the Q_L decreases to 717 and 523 mAh g^{-1} (57% and 41.5% of the theoretical Q_L) respectively. The above results reveal that the high loading of sulfur can decrease the capacity contribution both from the electrochemical reaction occurred at ~2.3 V and ~2.1 V. More interestingly, Q_L/Q_H is reduced from 2.64 to 1.95 with increasing the loading of S, indicating the slow liquid-to-solid reaction in kinetics occurred at ~2.1 V is more dependent on the loading of S and the electric conductivity of electrodes. In opposite, the increase of Q_H/Q_L with increasing sulfur loading reveals the fast solid-to-liquid redox reaction at ~2.3 V make more contributions for the capacity of electrodes with high sulfur loadings.

Fig. 8c shows the cyclic performances of the 3D-MPGF-S electrodes at 0.1C. To fully activate sulfur, the first discharge was performed at 0.05C. The 3D-MPGF-S2.5 electrode had the highest initial discharge capacity of 1187 mAh g^{-1} at 0.1C. The discharge capacity of 50th cycle decayed to 618 mAh g^{-1}, corresponding to retention of 52%. The Columbic efficiency was ~96.5%. The 3D-MPGF-S7 electrode delivered an initial capacity of 878 mAh g^{-1}. But at 50th cycle, the reversible capacity (513 mAh g^{-1}) still remained 58% of the initial capacity. The Coulombic efficiency was ~94.8%. When the sulfur loading increased to 13 mg cm^{-2}, the 3D-MPGF-S13 electrode displayed an initial capacity of 500 mAh g^{-1} and a lower Columbic efficiency of 94%, but higher capacity retention of

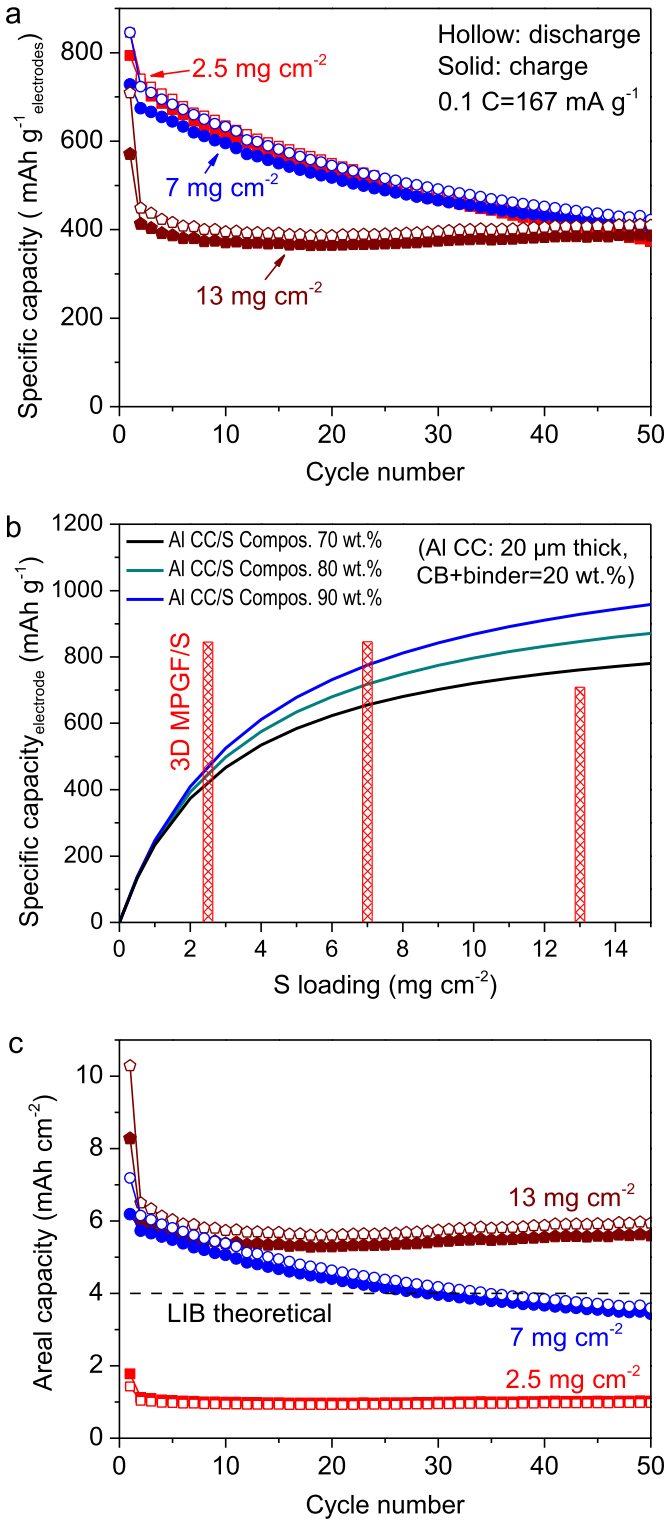

Fig. 9. (a) Specific capacities calculated based on overall weight of electrodes; (b) Comparison of 3D-MPGF/S electrodes with theoretical specific capacities of conventional electrodes of carbon black-S composites coated on Al CC with different sulfur contents (70–90 wt%) and different sulfur loadings (0–15 mg cm^{-2}); (c) The areal capacities of 3D-MPGF-S electrodes with different sulfur loadings. (A colour version of this figure can be viewed online.)

91.4% (457 mAh g^{-1}).

It can be observed from Fig. 8c that, although the reversible capacity decreases with increasing the loading of sulfur, the capacity retention increases. This is so because, at low sulfur loading, sulfur has higher initial utilization but also higher percentage of capacity loss due to the dissolution and migration of polysulfides through the unfilled channels (as seen in Fig. 6a). For high loading of S, due to the high resistivity of large sulfur aggregation, the activation of sulfur became lower, resulting in lower initial capacity. The high capacity retention could be mainly due to the reaction between sulfur and long-chain polysulfides, which is fast in kinetics and less dependent on the sulfur loading as abovementioned. In comparison with the low S-loading electrodes, the compensation of newly formed long-chain polysulfides from initially unused S would balance the lost long-chain polysulfides in electrolyte and make a contribution to the capacity. Yang et al. also reported the excellent capacity retention occurred in lithium/polysulfide semi-liquid battery [41]. In addition, a synergetic surface protection of lithium anode by the polysulfides/$LiNO_3$ can inhibit the corrosion and lithium dendrites formation on anodes and keep the cycling stable [41–44].

The electrochemical impedance spectroscopy (EIS) measurements were performed for a better understanding why the lower S-loading electrode exhibited higher reversible capacity than higher S-loading electrodes. Fig. 8d shows the Nyquist plots of the various 3D-MPGF-S electrodes. It demonstrates that with increasing the sulfur loading of electrodes from 2.5 to 7 mg cm^{-2}, the resistance of charge transfer R_{ct} slightly increases from 29.6 to 32.2 Ω. There is a large increase of R_{ct} to 65.3 Ω when the loading of sulfur is 13 mg cm^{-2}. The lower resistance of charger transfer reflects faster kinetics. It should also be noticed that the reason for the slight increase of R_{ct} for low S-loading (below 7 mg cm^{-2}) electrodes could be due to the good contact between sulfur and graphene. The trend shown in the charge transfer resistance is in good agreement with the reversible capacity.

It is important to evaluate the capacities based on overall electrodes because metal current collectors usually lower the practical specific capacity densities as they have higher mass densities. Fig. 9a shows the specific capacities of 3D-MPGF-S electrodes with different sulfur loadings. Interestingly, the 3D-MPGF-S2.5 and 3D-MPGF-S7 exhibited similar cyclic stabilities and capacities of electrodes. The initial discharge can reach an ultrahigh capacity of ~844 mAh g^{-1}. In contrast, the 3D-MPGF-S13 presents a lower initial practical capacity of 709 mAh g^{-1}. All the initial capacities of electrodes are much higher than those reported previously, see Table 1 [28,45–50]. It is more distinct to compare with the theoretical specific capacities of electrodes by using sulfur composites (sulfur content from 70% to 90%), Al foil current collectors (20 μm thick), carbon black (10 wt%) and binders (10 wt%) as shown in Fig. 9b. All the calculations are based on the theoretical capacity of sulfur 1675 mAh g^{-1}. It shows for an electrode of sulfur composite/Al CC, the specific capacity of electrode increases with raising the sulfur content and loading to offset the weight expense of Al current collector and other components such as carbon black (CB) and binders. For the same sulfur loading of 2.5 mg cm^{-2}, the real capacity of electrodes varies with the sulfur content but presents only 424–471 mAh g^{-1}, which is much lower than the capacity of the as-prepared 3D-MPGF-S electrode. Even after 50 cycles, the capacities of all 3D-MPGF-S electrodes can still remain at ~400 mAh g^{-1}, which is also superb to most reported electrodes (see Table 1). It should be also pointed out that it is a huge challenge to reach the theoretical specific capacity of sulfur 1675 mAh g^{-1} without decay during cycling. So employing the lightweight carbon based current collectors in sulfur batteries could be a good and easier strategy for achieving highest capacity of electrodes for large-scale application. The excellent high capacities of electrodes are mainly attributed to the low density and conductive networks of 3D-MPGF.

We also evaluated the areal capacities of 3D-MPGF-S electrodes, as seen in Fig. 9c. The 3D-MPGF-S13 electrode reached an initial areal capacity of 10.3 mAh cm^{-2}, which is higher than most reported values [28,45–50]. After 50 cycles its areal capacity remained at 5.9 mAh cm^{-2}, which is still higher than the areal capacity of $LiCoO_2$ cathodes (~4 mAh cm^{-2}) and other carbon/sulfur electrodes (see Table 1) [28,45–50]. In comparison, the 3D-MPGF-S7 electrode initially displayed an areal capacity of 7.2 mAh cm^{-2}, but decayed fast to below 4 mAh cm^{-2} by 30th cycle. Due to the low sulfur loading, the 3D-MPGF-S2.5 electrode only presented 1–2 mAh cm^{-2}. The high areal capacities of 3D-MPGF-S13 are mainly due to the high specific capacities by using 3D-MPGF and high loading of sulfur.

For electrode with high S loading, reversible capacity decreased while capacity retention increased, while the opposite is observed for low S loading electrode. This implies a trade-off between the capacity retention and utilization of sulfur at different sulfur loadings. Lower loading of sulfur shows higher reversible capacity attributed to better utilization of sulfur. However, from the viewpoint of the specific capacity and areal capacity of overall electrodes, higher loading of sulfur performs more promising in practice. An optimum performance can be obtained when the loading of sulfur is around 7 mg cm^{-2}, see Fig. 9. To achieve a high reversible capacity and capacity retention of electrodes at high S loading, improving the electric conductivity, reducing the dissolution and migration of polysulfides are of importance. Moreover, accelerating the kinetics of the lower-plateau reaction in particular

Table 1
A comparison of capacitive performances based on weight of electrodes and areal capacity between this work and other previously reported porous graphene/sulfur(/Al) electrodes.

Electrodes	S loading (mg cm^{-2})	Electrode weight capacity (mAh g^{-1})		Areal capacity (mAh cm^{-2})		Ref.
		initial	50th cycle	initial	50th cycle	
3D N-doped G-nanomesh/S/Al	1.0	120 at 0.2C	94 at 0.2C	1.06	0.83	[45]
3D G sponges/S	2.0	805 at 0.1C	652 at 0.1C	2.96	~2.4	[46]
rGO foam/S/Al	~1.2	~165 at 0.1C	103 at 0.5C	1.5	~0.94	[28]
3D G/S/Al	6.3	390 at 0.2C	314 at 0.2C	5.1	4.1	[47]
S/FLG foam[a]	2.0	426 at~0.5C	270 at~0.5C	1.64	1.04	[48]
GMS[b]/S/CNT	2.5	588 at 0.033C	443 at 0.2C	2.67	2.14	[49]
Porous G/S/Al	2.0	434 at 0.5C	384 at 0.5C	2.1	1.6	[50]
3D-MPGF-S	2.5	844 at 0.05C	387 at 0.1C	1.8	1.0	This work
	7	845 at 0.05C	422 at 0.1C	7.2	3.6	
	13	709 at 0.05C	409 at 0.1C	10.3	5.9	

[a] Few layer graphene foam.
[b] Graphene micro-sphere.

for high-sulfur-loading electrodes could significantly increase the reversible capacity. It is expected that the cyclic performances of 3D-MPGF-S with high sulfur loading can be improved further by structural modification, surface functionalization or employing functional separators between 3D-MPGF-S cathodes and lithium anodes in future works. So far the free-standing 3D-MPGF exhibits already superior advantages as lightweight binder-free current collectors to increase the specific capacities of electrodes.

4. Conclusion

In summary, 3D micron-porous graphene foams are synthesized by a novel one-route heating process starting from nickel or iron salts precursors. The method is facile, fast and sustainable due to the combination of synthesis of micron-porous metals and growth of graphene, and recycling of metallic waste. The as-synthesized graphene foams exhibit free-standing, low density and micron-porous porous structure. Different wall thicknesses and graphitization of porous graphene can be achieved by changing the CVD time.

The micron-porous graphene foams are tested as binder-free current collectors of sulfur cathodes. 3D-MPGF-S electrodes deliver high specific capacities of electrodes and areal capacity densities. It is also found that the loading of sulfur closely influences the utilization of sulfur and the electrochemical reactions, especially the slow kinetical reaction at ~2.1 V, because of the increased resistance of electron transport between graphene and sulfur species. The as-developed 3D micron-porous graphene foam is a promising electrode material for various anodic and cathodic electrodes (e.g. Li, Si, Sn, lithium iron phosphate etc.) of batteries and supercapacitors.

Acknowledgement

The authors gratefully acknowledge the financial support from the Faculty of Science and Engineering, University of Groningen, The Netherlands. We also sincerely thank Professor Wesley R. Browne for valuable discussion and support to the Raman analysis of graphene samples.

Appendix A. Supplementary data

Supplementary data to this article can be found online at https://doi.org/10.1016/j.carbon.2018.12.103.

References

[1] Z.W. Seh, Y.M. Sun, Q.F. Zhang, Y. Cui, Designing high-energy lithium–sulfur batteries, Chem. Soc. Rev. 45 (2016) 5605–5634.
[2] S. Evers, L.F. Nazar, New approaches for high energy density lithium–sulfur battery cathodes, Acc. Chem. Res. 46 (2013) 1135–1143.
[3] Y.X. Yin, S. Xin, Y.G. Guo, L.J. Wan, Lithium–sulfur batteries: electrochemistry, materials, and prospects, Angew. Chem. Int. Ed. 52 (2013) 13186–13200.
[4] Z. Li, L.X. Yuan, Z.Q. Yi, Y. Liu, Y. Xin, Z.L. Zhang, Y.H. Huang, A dual coaxial nanocable sulfur composite for high rate lithium–sulfur batteries, Nanoscale 6 (2014) 1653–1660.
[5] F.Y. Jin, S. Xiao, L.J. Lu, Y. Wang, Efficient activation of high-loading sulfur by small CNTs confined inside a large CNT for high-capacity and high-rate lithium–sulfur batteries, Nano Lett. 16 (2016) 440–447.
[6] G.J. Hu, C. Xu, Z.H. Sun, S.G. Wang, H.M. Cheng, F. Li, W.C. Ren, 3D graphene-foam–reduced-graphene-oxide hybrid nested hierarchical networks for high-performance Li–S batteries, Adv. Mater. 28 (2016) 1603–1609.
[7] L.Q. Lu, L.J. Lu, Y. Wang, Sulfur film-coated reduced graphene oxide composite for lithium–sulfur batteries, J. Mater. Chem. 1 (2013) 9173–9181.
[8] W.Y. Li, Q.F. Zhang, G.Y. Zheng, Z.W. Seh, H.B. Yao, Y. Cui, Understanding the role of different conductive polymers in improving the nanostructured sulfur cathode performance, Nano Lett. 13 (2013) 5534–5540.
[9] W.Y. Li, G.Y. Zheng, Y. Yang, Z.W. Seh, N. Liu, Y. Cui, High-performance hollow sulfur nanostructured battery cathode through a scalable, room temperature, one-step, bottom-up approach, Proc. Natl. Acad. Sci. Unit. States Am. 110 (2013) 7148–7153.
[10] L.Q. Lu, N. Schriever, J.Th M. De Hosson, Y.T. Pei, Low-temperature solid-state growth of three-dimensional bicontinuous nanoporous graphene with tunable porosity for lithium–sulfur batteries, J. Mater. Chem. 6 (2018) 11405–11415.
[11] W.Z. Bao, X.Q. Xie, J. Xu, X. Guo, J.J. Song, W.J. Wu, D.W. Su, G.X. Wang, Confined sulfur in 3D MXene/reduced graphene oxide hybrid nanosheets for lithium–sulfur battery, Chem. Eur J. 23 (2017) 12613–12619.
[12] X. Liu, J.Q. Huang, Q. Zhang, L.Q. Mai, Nanostructured metal oxides and sulfides for lithium–sulfur batteries, Adv. Mater. 29 (2017) 1601759.
[13] M.A. Pope, I.A. Aksay, Structural design of cathodes for Li–S Batteries, Adv. Energy Mater. 5 (2015) 1500124.
[14] A. Eftekhari, D.-W. Kim, Cathode materials for lithium–sulfur batteries: a practical perspective, J. Mater. Chem. 5 (2017) 17734–17776.
[15] Z.X. Cao, J. Zhang, Y.M. Ding, Y.L. Li, M.J. Shi, H.Y. Yue, Y. Qiao, Y.H. Yin, S.T. Yang, In situ synthesis of flexible elastic N-doped carbon foam as a carbon current collector and interlayer for high-performance lithium sulfur batteries, J. Mater. Chem. 4 (2016) 8636–8644.
[16] C. Hu, C. Kirk, J. Silvestre-Albero, F. Rodríguez-Reinosoc, M.J. Biggs, Free-standing compact cathodes for high volumetric and gravimetric capacity Li–S batteries, J. Mater. Chem. 5 (2017) 19924–19933.
[17] M.D. Patel, E. Cha, C. Kang, B. Gwalani, W. Choi, High performance rechargeable Li–S batteries using binder-free large sulfur-loaded three-dimensional carbon nanotubes, Carbon 118 (2017) 120–126.
[18] P.Y. Zhai, J.Q. Huang, L. Zhu, J.L. Shi, W. Zhu, Q. Zhang, Calendering of free-standing electrode for lithium–sulfur batteries with high volumetric energy density, Carbon 111 (2017) 493–501.
[19] R.P. Fang, S.Y. Zhao, P.X. Hou, M. Cheng, S. Wang, H.-M. Cheng, C. Liu, F. Li, 3D interconnected electrode materials with ultrahigh areal sulfur loading for Li–S batteries, Adv. Mater. 28 (2016) 3374–3382.
[20] C. Luo, H.L. Zhu, W. Luo, F. Shen, X.L. Fan, J.Q. Dai, et al., Atomic-layer-deposition functionalized carbonized mesoporous wood fiber for high sulfur loading lithium sulfur batteries, ACS Appl. Mater. Interfaces 9 (2017) 14801–14807.
[21] X. Yao, Y.L. Zhao, Three-dimensional porous graphene networks and hybrids for lithium–ion batteries and supercapacitors, Chem 2 (2017) 171–200.
[22] Y.F. Ma, Y.S. Chen, Three-dimensional graphene networks: synthesis, properties and applications, Natl Sci. Rev. 2 (2015) 40–53.
[23] H. Bi, T.Q. Lin, F. Xu, Y.F. Tang, Z.Q. Liu, F.Q. Huang, New graphene form of nanoporous monolith for excellent energy storage, Nano Lett. 16 (2016) 349–354.
[24] Y. Ito, Y. Tanabe, J.H. Han, T. Fujita, K. Tanigaki, M.W. Chen, Multifunctional porous graphene for high-efficiency steam generation by heat localization, Adv. Mater. 27 (2015) 4302–4307.
[25] Y.F. Tang, F.Q. Huang, H. Bi, Z.Q. Liu, D.Y. Wan, Highly conductive three-dimensional graphene for enhancing the rate performance of $LiFePO_4$ cathode, J. Power Sources 203 (2012) 130–134.
[26] H.X. Ji, L.L. Zhang, M.T. Pettes, H.F. Li, S.S. Chen, L. Shi, R. Piner, R.S. Ruoff, Ultrathin graphite foam: a three-dimensional conductive network for battery electrodes, Nano Lett. 12 (2012) 2446–2451.
[27] J.S. Luo, J.L. Liu, Z.Y. Zeng, C.F. Ng, L.J. Ma, H. Zhang, J.Y. Lin, Z.X. Shen, H.J. Fan, Three-dimensional graphene foam supported Fe_3O_4 lithium battery anodes with long cycle life and high rate capability, Nano Lett. 13 (2013) 6136–6143.
[28] W. Deng, X.F. Zhou, Q.L. Fang, Z.P. Liu, Graphene/sulfur composites with a foam-like porous architecture and controllable pore size for high performance Lithium–Sulfur batteries, ChemNanoMat 2 (2016) 952–958.
[29] H.P. Cong, J.F. Chen, S.H. Yu, Graphene-based macroscopic assemblies and architectures: an emerging material system, Chem. Soc. Rev. 43 (2014) 7295–7325.
[30] Z.Y. Lyu, L.J. Yang, D. Xu, J. Zhao, H.W. Lai, Y.F. Jiang, Q. Wu, Y. Li, X.Z. Wang, Z. Hu, Hierarchical carbon nanocages as high-rate anodes for Li– and Na–ion batteries, Nano Res 8 (2015) 3535–3543.
[31] L.R. Shi, K. Chen, R. Du, A. Bachmatiuk, M.H. Rümmeli, K.W. Xie, Y.Y. Huang, Y.F. Zhang, Z.F. Liu, Scalable seashell-based chemical vapor deposition growth of three-dimensional graphene foams for oil–water separation, J. Am. Chem. Soc. 138 (2016) 6360–6363.
[32] Y. Ito, Y. Tanabe, H.J. Qiu, K. Sugawara, S. Heguri, N.H. Tu, K.K. Huynh, T. Fujita, T. Takahashi, K. Tanigaki, M.W. Chen, High-quality three-dimensional nanoporous graphene, Angew. Chem. 126 (2014) 4922–4926.
[33] K.Q. Qin, E.Z. Liu, J.J. Li, J.L. Kang, C.S. Shi, C.N. He, F. He, N.Q. Zhao, Free-standing 3D nanoporous duct-like and hierarchical nanoporous graphene films for micron-level flexible solid-state asymmetric supercapacitors, Adv. Energy Mater. 6 (2016) 1600755.
[34] L.Q. Lu, P. Andela, J.T.M. De Hosson, Y.T. Pei, Template-free synthesis of nanoporous nickel and alloys as binder-free current collectors of Li ion batteries, ACS Appl. Nano Mater. 1 (2018) 2206–2218.
[35] L.J. van der Pauw, A method of measuring specific resistivity and Hall effect of discs of arbitrary shape, Philips Res. Rep. 13 (1958) 1–9.
[36] J.J. Lander, H.E. Kern, A.L. Beach, Solubility and diffusion coefficient of carbon in nickel: reaction rates of nickel-carbon alloys with barium oxide, J. Appl. Phys. 23 (1952) 1305.
[37] Z.P. Chen, W.C. Ren, L.B. Gao, B.L. Liu, S.F. Pei, H.M. Cheng, Three-dimensional flexible and conductive interconnected graphene networks grown by chemical vapour deposition, Nat. Mater. 10 (2011) 424–428.
[38] L.G. Cançado, K. Takai, T. Enoki, General equation for the determination of the

crystallite size La of nanographite by Raman spectroscopy, Appl. Phys. Lett. 88 (2006) 163106.
[39] H.J. Qiu, Y. Ito, W. Cong, Y.W. Tan, P. Liu, A. Hirata, et al., Nanoporous graphene with single-atom nickel dopants: an efficient and stable catalyst for electrochemical hydrogen production, Angew. Chem. Int. Ed. 54 (2015) 14031–14035.
[40] Y.Z. Xue, B. Wu, Y.L. Guo, L.P. Huang, L. Jiang, J.Y. Chen, D.C. Geng, Y.Q. Liu, W.P. Hu, G. Yu, Synthesis of large-area, few-layer graphene on iron foil by chemical vapor deposition, Nano Res 4 (2011) 1208–1214.
[41] Y. Yang, G.Y. Zheng, Y. Cui, A membrane-free lithium/polysulfide semi-liquid battery for large-scale energy storage, Energy Environ. Sci. 6 (2013) 1552–1558.
[42] W.Y. Li, H.B. Yao, K. Yan, G.Y. Zheng, Z. Liang, Y.M. Chiang, Y. Cui, The synergetic effect of lithium polysulfide and lithium nitrate to prevent lithium dendrite growth, Nat. Commun. 6 (2015) 7436.
[43] S.S. Zhang, Liquid electrolyte lithium/sulfur battery: fundamental chemistry, problems, and solutions, J. Power Sources 231 (2013) 153–162.
[44] D. Aurbach, E. Pollak, R. Elazari, G. Salitra, C.S. Kelley, J. Affinito, On the surface chemical aspects of very high energy density, rechargeable Li–Sulfur batteries, J. Electrochem. Soc. 156 (2009) A694–A702.
[45] C. Li, X.L. Sui, Z.B. Wang, Q. Wang, D.M. Gu, 3D N-doped graphene nanomesh foam for long cycle life lithium–sulfur Battery, Chem. Eng. J. 326 (2017) 265–272.
[46] C. Lin, C.J. Niu, X. Xu, K. Li, Z.Y. Cai, Y.L. Zhang, X.P. Wang, L.B. Qu, Y.X. Xu, L.Q. Mai, A facile synthesis of three-dimensional graphene sponge composited with sulfur nanoparticles for flexible Li–S cathodes, Phys. Chem. Chem. Phys. 18 (2016) 22146–22153.
[47] J. Wang, S. Cheng, W.F. Li, S. Zhang, H.F. Li, Z.Z. Zheng, F.J. Li, L.Y. Shi, H.Z. Lin, Y.G. Zhang, Simultaneous optimization of surface chemistry and pore morphology of 3D graphene–sulfur cathode via multi-ion modulation, J. Power Sources 321 (2016) 193–200.
[48] K. Xi, P.R. Kidambi, R.J. Chen, C.L. Gao, X.Y. Peng, C. Ducati, S. Hofmann, R.V. Kumar, Binder free three-dimensional sulphur/few-layer graphene foam cathode with enhanced high-rate capability for rechargeable lithium sulphur batteries, Nanoscale 6 (2014) 5746–5753.
[49] J.L. Shi, H.J. Peng, L. Zhu, W.C. Zhu, Q. Zhang, Template growth of porous graphene microspheres on layered double oxide catalysts and their applications in lithium–sulfur batteries, Carbon 92 (2015) 96–105.
[50] C. Tang, B.Q. Li, Q. Zhang, L. Zhu, H.F. Wang, J.L. Shi, F. Wei, CaO-templated growth of hierarchical porous graphene for high-power lithium–sulfur battery applications, Adv. Funct. Mater. 26 (2016) 577–585.